Interface focus

J. R. Soc. Interface (2009) **6**, S587–S597
doi:10.1098/rsif.2009.0142.focus
Published online 17 June 2009

Rastering strategy for screening and centring of microcrystal samples of human membrane proteins with a sub-10 μm size X-ray synchrotron beam

Vadim Cherezov[1,*], Michael A. Hanson[1], Mark T. Griffith[1], Mark C. Hilgart[3], Ruslan Sanishvili[3], Venugopalan Nagarajan[3], Sergey Stepanov[3], Robert F. Fischetti[3], Peter Kuhn[2] and Raymond C. Stevens[1]

[1]*Department of Molecular Biology, and* [2]*Department of Cell Biology, Scripps Research Institute, La Jolla, CA 92037, USA*
[3]*GM/CA CAT at the APS, Biosciences Division, Argonne National Laboratory, Argonne, IL 60439, USA*

Crystallization of human membrane proteins in lipidic cubic phase often results in very small but highly ordered crystals. Advent of the sub-10 μm minibeam at the APS GM/CA CAT has enabled the collection of high quality diffraction data from such microcrystals. Herein we describe the challenges and solutions related to growing, manipulating and collecting data from optically invisible microcrystals embedded in an opaque frozen *in meso* material. Of critical importance is the use of the intense and small synchrotron beam to raster through and locate the crystal sample in an efficient and reliable manner. The resulting diffraction patterns have a significant reduction in background, with strong intensity and improvement in diffraction resolution compared with larger beam sizes. Three high-resolution structures of human G protein-coupled receptors serve as evidence of the utility of these techniques that will likely be useful for future structural determination efforts. We anticipate that further innovations of the technologies applied to microcrystallography will enable the solving of structures of ever more challenging targets.

Keywords: lipidic cubic phase; G protein-coupled receptor; minibeam; microcrystallography

1. INTRODUCTION

One of the bottlenecks in structural studies of membrane proteins is obtaining diffraction quality crystals. Perhaps even more challenging are proteins with low ratio of hydrophilic to hydrophobic surface area such as G protein-coupled receptors (GPCRs). Crystallization in lipidic cubic phase (LCP; Landau & Rosenbusch 1996) is advantageous for promoting crystal packing contacts between hydrophilic as well as between hydrophobic protein surfaces (Caffrey 2009). Crystals grown in LCP, also referred as *in meso* crystallization (Caffrey 2003), are in general well ordered probably because of the increase in available crystal packing area and diffusion driven mechanism; however, on average, these crystals have a smaller size than the typical crystals grown in aqueous solution. In certain cases, it has not been possible to obtain crystals larger than approximately 1000 μm^3, a volume that would contain approximately 10^9 unit cells. Despite surprisingly good diffraction limits, such crystals present a significant challenge for standard crystallographic techniques in that detection of the crystals in the drop, harvesting and collecting high quality diffraction data become non-trivial and a feat nearly impossible without the development of microcrystallography techniques.

Microcrystallography emerged and gained popularity more than a decade ago with the appearance of high brilliance beams at the third generation synchrotron sources. Much of the pioneering work was done at ID-13 at the ESRF (Pebay-Peyroula *et al.* 1997). The development of a micro-diffractometer at the EMBL-Grenoble (Perrakis *et al.* 1999) paved the way for routine microcrystallography experiments. Small X-ray beams with diameters less than 10 μm have been used to collect data from thin needles (Rasmussen

*Author for correspondence (vcherezo@scripps.edu).

One contribution of 13 to a Theme Supplement 'Biological physics at large facilities'.

Received 15 April 2009
Accepted 21 May 2009

et al. 2007) and small microcrystals (Coulibaly *et al.* 2007), as well as to improve diffraction from inhomogeneous (Sanishvili *et al.* 2008) or mosaic (Xiao *et al.* 2003) crystals.

The General Medical Sciences and Cancer Institute Collaborative Access Team (GM/CA CAT) at the Advance Photon Source, Argonne, IL, USA, has developed a dedicated protein microcrystallography minibeam apparatus (Fischetti *et al.* 2009). A systematic feasibility study using this apparatus for data collection from test crystals measuring less than $10 \times 10 \times 10\ \mu m^3$ has been published (Sanishvili *et al.* 2008). Here we report the results of a collaboration between the Cherezov–Kuhn–Stevens groups at The Scripps Research Institute (TSRI) and APS GM/CA CAT to develop advanced methods to centre optically invisible crystals and collect high quality diffraction data. The group at Argonne developed the automated software to raster search a user defined sample volume using the GM/CA minibeam. The groups at TSRI developed improved methods for growing and harvesting *in meso* grown GPCR microcrystals, conducted the manual rastering of optically invisible crystals, provided valuable feedback on the automated rastering capability and developed data collection strategies to mitigate the effects of radiation damage.

2. MATERIAL AND METHODS

2.1. Protein expression and purification

Human β_2-adrenergic GPCR (β_2AR) was engineered by replacing part of the intracellular loop 3 with lysozyme from T4 phage (β_2AR-T4L) in order to improve the receptor's stability and increase its chances for successful crystallization (Rosenbaum *et al.* 2007). Initial purified β_2AR-T4L protein, in which residues Gln231–Ser262 were replaced with residues 2–161 of T4 lysozyme, the C-terminus was truncated at Gly365 and one glycosylation site was eliminated through Asn187 to Glu mutation, was obtained from B. Kobilka (Stanford University). Thermally stabilized β_2AR-T4L construct (β_2AR(E122W)-T4L) and human adenosine A_{2A} receptor T4L fusion construct (A_{2A}R-T4L) were designed, cloned, expressed and purified in house (Hanson *et al.* 2008; Jaakola *et al.* 2008). In β_2AR(E122W)-T4L, residues Gln231–Ser262 were replaced with residues 2–161 of T4 lysozyme, the C-terminus was truncated at Lys348, one glycosylation site was eliminated through Asn187 to Glu mutation and Glu122Trp mutation (Roth *et al.* 2008) was introduced to increase the stability. In A_{2A}R-T4L, residues Leu209–Ala221 were replaced with residues 2–161 of T4 lysozyme and the C-terminus was truncated at Ala316.

The constructs were generated using standard cloning techniques and recombinantly expressed in baculovirus infected sf9 insect cells as described in detail in Rosenbaum *et al.* (2007), Hanson *et al.* (2008) and Jaakola *et al.* (2008). The cells were harvested 48 h after infection and disrupted by a nitrogen cavitation bomb. The cell membranes were isolated and washed using repeated centrifugation followed by resuspension and homogenization. The protein was solubilized from the membranes using 0.5 per cent (w/v) *n*-dodecyl-β-D-maltopyranoside/0.01 per cent (w/v) cholesterol hemisuccinate (CHS) and purified with Talon (Clonetech) and Ni Sepharose (GE LifeScience) IMAC columns. PNGase F (New England Biolabs) was used on the Ni Sepharose column to de-glycosylate the protein. After elution from the Ni Sepharose column, the protein was concentrated to 30–70 mg ml^{-1} using a 100 kDa cutoff Vivaspin concentrator (Sartorius).

The final protein samples were of high purity (>95% by SDS–PAGE) and displayed a single monomer peak on an analytical size exclusion chromatography column.

2.2. *Robotic* in meso *crystallization setup*

Protein solution at 30–70 mg ml^{-1} concentration was mixed with a lipid (typically monoolein or monoolein supplemented with 5–10 wt% of cholesterol or other lipids) in the ratio of two parts of protein solution to three parts of lipid using a syringe lipid mixer (Cheng *et al.* 1998). After a clear homogeneous LCP was formed, it was transferred into a 100 µl gas-tight syringe (Hamilton Company). A short 10 mm removable needle (gauge 26) was attached to the syringe and the syringe was mounted on an *in meso* crystallization robot (Cherezov *et al.* 2004). The robot dispensed 25–50 nl of protein-laden cubic phase and 0.8 µl of precipitant solution per well of a 96-well glass sandwich plate (Cherezov *et al.* 2004). The wells were sealed with a cover glass using a brayer. All manipulations on setting up crystallization trials were performed at room temperature (21–23°C). After the plates were sealed, they were transferred into an incubator/imager (RockImager 1000, Formulatrix), where they were stored at 20°C and imaged according to a specified schedule (typically on 0, 1, 3, 5, 7, 10, 14, 21 and 31 days after setup).

2.3. Crystal harvesting

Crystals were harvested directly from the glass sandwich plates. All operations were performed under a variable zoom stereo microscope (Nikon SMZ1500). To open an individual well, the cover glass was scored using a sharp corner of a glass capillary cutting stone (Hampton Research, cat# HR4-334) with four short strokes forming a square centred inside the well boundaries. Strong sharp point tweezers (Ted Pella, cat# 510) were used to press around the scored perimeter to propagate the scratch through the thickness of the cover glass. Then two holes were punched at two opposite corners of the square, followed by an injection of 2–3 µl of precipitant solution through one of the holes inside the well to reduce dehydration during the well opening manipulations. A sharp angled needle probe (Ted Pella, cat# 13650) was used to free the glass square and carefully lift it up. An extra 5 µl of precipitant solution was added on top of the opened well. The crystals were harvested directly from the LCP using MicroMounts (MiTeGen) with the diameter matching the crystal size (typically 30 µm). A polarizer and analyser attached to the microscope were used at close to cross at 90° orientation to facilitate visualization of birefringent crystals while still providing enough light to see

the MicroMount approaching the crystal. The amount of the lipid phase surrounding the harvested crystal was minimized as much as possible. If the crystal was sitting deep inside the LCP bolus, a MicroMount was used to remove the top LCP layer and expose the crystal at the surface, after which another clean MicroMount was used to harvest the crystal. The harvested crystal was immediately plunged into liquid nitrogen. As the precipitant contained at least 25 per cent PEG400, it protected the crystal during the freezing and no additional cryoprotectant was used.

2.4. Loop rastering and crystal centring

Optically invisible microcrystals were located and centred in the minibeam using diffraction from a highly attenuated X-ray beam to minimize radiation damage. A manual centring procedure was developed initially and later it was replaced by an automatic raster scanning. Both these approaches are described in this section.

2.4.1. Manual centring. As the loop size was in general significantly larger than the size of the minibeam, the whole loop area was initially scanned using a beam with a cross section of $69 \times 21\ \mu m^2$ (full width at half maximum, FWHM) at the sample position. The beam size was defined by slits that were located 230 mm upstream of the sample position and were set to $75 \times 25\ \mu m^2$ defining the beam that was focused at the sample position. The beam was attenuated 20-fold to minimize radiation damage. When diffraction was observed the corresponding area was coarsely scanned with a 20-fold attenuated minibeam using 10 μm steps and consequently fine tuned using 2 μm steps with a 10-fold attenuated minibeam. During the fine tuning, the integrated intensity within a strongly diffracting spot served as feedback for selecting the best position. The direction of the crystal motion during the fine tuning was determined by the gradient descent method, which allowed a minimum number of steps but could also potentially lead to a local minima trap, especially in the case of larger crystals. After the crystal was centred in one orientation, the loop was rotated 90° and the coarse 10 and fine 2 μm scans were repeated in the direction perpendicular to the rotation axis. The alignment of each crystal took 30–60 min and exposed the crystal to a total X-ray dose of <1 MGy, which was equivalent to <1 s exposure with unattenuated beam.

2.4.2. Automatic rastering. Automatic rastering of samples was developed as a tool invoked within the GM/CA CAT adaptation of Blu-Ice (McPhillips *et al.* 2002; Stepanov *et al.* 2006). A similar tool was developed in the original Blu-Ice for automated centring (Song *et al.* 2007) of larger crystals with larger X-ray beams. The rastering tool developed at GM/CA CAT uses the minibeam to centre optically invisible crystals in the X-ray beam and to map better ordered regions of large crystals. The user can choose to collect data from the best part of the crystal using the full focused beam (or that defined by the upstream slits) as was suggested earlier (Sanishvili *et al.* 2008) or to collect partial datasets by walking along the crystal with the minibeam. At present, automated rastering follows manual centring of the loop on the crosshairs where the X-ray beam is also centred independently. To minimize the number of exposures during rastering of optically independent crystals, it is recommended to rotate the sample mount so that its smallest profile is rastered first.

Automated rastering starts with larger steps and the beam defined by slits, as described above for manual rastering. The initial grid parameters are entered in the raster tab of Blu-Ice-EPICS, and the resulting grid is displayed over the sample image. On clicking start, diffraction images are taken for each cell in the grid. No search optimization is currently done.

Diffraction images are analysed with DISTL (Zhang *et al.* 2006) on the fly and/or by a user manually with image viewing software. DISTL produces per-image quality indicators including spot total and ice rings. The indicators are displayed in sortable columns in the results table. Processing with DISTL is done in the background on a SAN-connected workstation and produces results at the same pace as rastering. With a 0.5 s exposure time this rate is 15 frames min^{-1}.

The user can select the grid point with the best diffraction as determined by DISTL by double clicking on the image identifier in the list prepared by the software. The centre of the cell of the corresponding grid point is then automatically centred.

For rastering with finer steps (≤10 μm), the user can select the 5 or 10 μm beam from a pull-down menu in the GM/CA CAT version of Blu-Ice. Once the sample is centred in the given plane, it is rotated by 90° and a single vertical scan is carried out with the minimum step size used in the previous scan. Exposure times and attenuation are selected as a compromise to achieve detectable diffraction while minimizing X-ray induced radiation damage to the sample. The total estimated dose absorbed by the crystal during a typical automatic rastering is less than 0.5 MGy.

2.5. Data collection and processing

X-ray data were collected on beamline 23ID-B at GM/CA CAT at the Advanced Photon Source, Argonne, IL, using a minibeam with a wavelength of 1.033 Å (12.000 keV) passing through a 10 μm collimator (Sanishvili *et al.* 2008; Fischetti *et al.* 2009) and a MarMosaic 300 CCD detector (Rayonix, Evanston, IL; formerly Mar USA). The minibeam in the earlier experiments before February 2008 had an oval shape with a size of $7.8 \times 6.3\ \mu m^2$ FWHM at the sample position as measured by a knife-edge scan, and with a total flux of 1×10^{11} photons s^{-1} $(100\ mA)^{-1}$, measured with an ion chamber (Sanishvili *et al.* 2008). Since February 2008, a new 10 μm collimator was used producing a $10.6 \times 11.6\ \mu m^2$ beam with an intensity of 2.2×10^{11} photons s^{-1} $(100\ mA)^{-1}$ at the sample position (Fischetti *et al.* 2009).

Data were integrated, scaled and merged using XDS (Kabsch 1993). Initial phase information was obtained by molecular replacement with Phaser (McCoy 2007) using the coordinates of T4 lysozyme and a polyalanine model of the rhodopsin 7 transmembrane (TM) helical bundle. Refinement was performed iteratively with

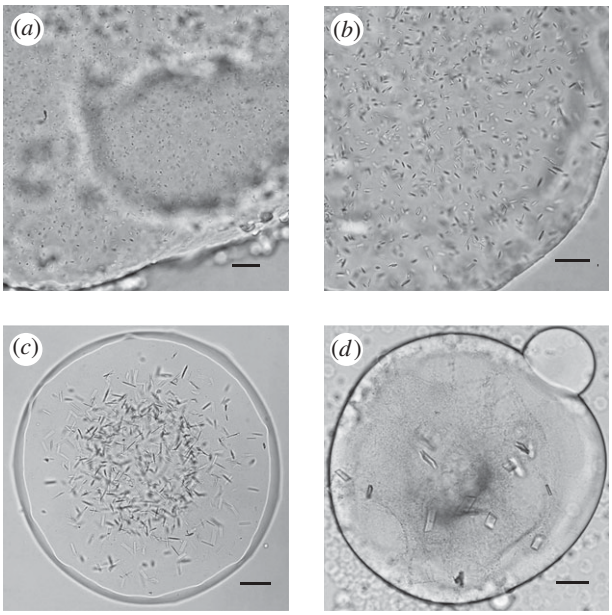

Figure 1. Improvements in size and shape of β_2AR-T4L crystals as the result of optimizations of crystallization conditions. (*a*) Initial crystals appearing as showers of microneedles with largest dimension of a few micrometres. (*b*) Crystals achieved after optimization of concentrations of the main precipitant (PEG 400), salt (sodium sulphate) and pH of the buffer. (*c*) Crystals obtained after optimization of the lipid additives. (*d*) Final crystals diffracting to high resolution. Scale bars, 25 μm (*a*,*b*); 50 μm (*c*,*d*).

Refmac5 (Murshudov *et al.* 1997), Phenix (Adams *et al.* 2002) and manual rebuilding in Coot (Emsley & Cowtan 2004).

3. RESULTS AND DISCUSSION

3.1. In meso *crystallization*

All GPCR crystals for this work were obtained using automated nanolitre *in meso* crystallization (Cherezov *et al.* 2004). Robotic setup allowed for extensive screening and optimization while consuming minimal amounts of protein. As little as 10 μl of concentrated protein solution (the minimal volume achievable with commercial centrifugation-based concentrators) was sufficient to perform 700–800 trials.

Unoptimized conditions generally produce crystals *in meso* appearing as showers of extremely small microcrystals (figure 1*a*). Detection of such tiny colourless protein crystals from within the LCP background is challenging. However, the glass sandwich plates in which the crystallization trials are set up in Cherezov *et al.* (2004) provide a superior optical environment for obtaining high-quality crystal images using a microscope with both bright-field illumination and cross-polarization capability (figures 1–3). Trace labelling proteins with a fluorescent dye are also useful for initial crystal detection (figure 2*c*). Alternatively a UV-fluorescence microscope can be used to both detect microcrystals in the low background LCP and confirm that they contain protein (figure 3*c*).

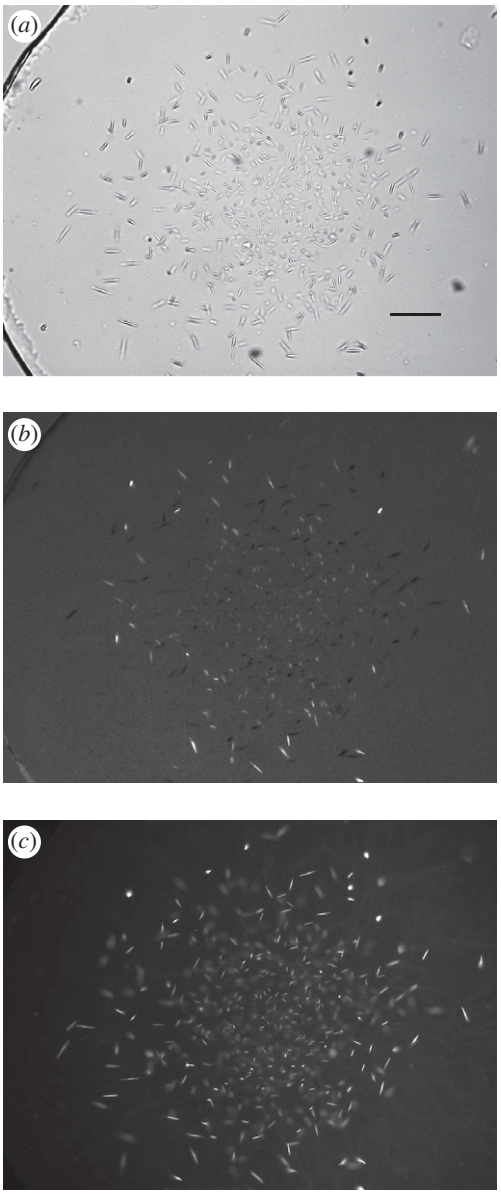

Figure 2. Imaging of small A_{2A}R-T4L crystals in LCP. (*a*) Image recorded with a Zeiss AxioImager microscope using a 10× objective and a bright-field illumination. LCP is very homogeneous and crystals are easily detected (scale bar, 25 μm). To confirm that the crystals are made of protein, the protein was labelled with a dye and fluorescence image was taken in (*c*). (*b*) Image recorded with a Zeiss AxioImager microscope using a 10× objective and crossed polarizers. Crystals show good birefringency, which also depends on their orientation in LCP. (*c*) Image recorded with a Zeiss AxioImager microscope using an epi-illumination with an excitation filter centred at 543 nm with a bandwidth of 22 nm and an emission filter with transmission between 575 and 640 nm. The protein was labelled with Cy3 succinimidyl ester at a trace ratio of below 1%. The fluorescence image provides a very good contrast even for very small, micrometre-size, crystals, confirming that the crystals contain protein.

Optimization of *in meso* crystallization conditions involves adjustment of many of the same parameters as one would explore in a typical crystallization experiment in an aqueous solution (Benvenuti & Mangani 2007). In addition, the identity of the host lipid and the identity and concentration of lipid-like or

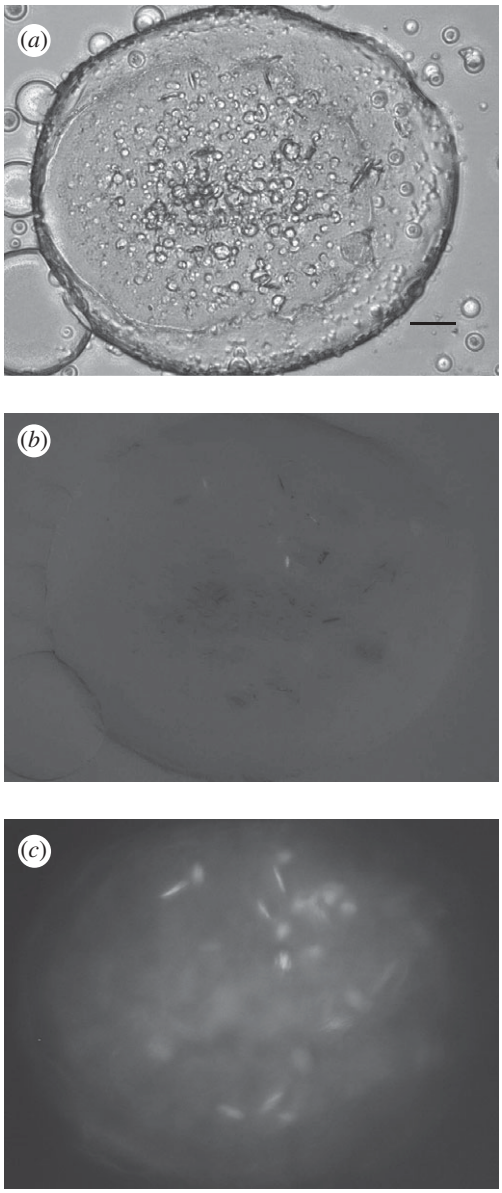

Figure 3. Imaging of small β_2AR-T4L crystals in LCP. (*a*) Image recorded with RockImager 1000 (Formulatrix) using a bright-field illumination. LCP contains many defects and irregularities scattering light and obscuring crystal detection. Scale bar, 50 μm. (*b*) Image recorded with RockImager 1000 using crossed polarizers. Crystals in this case display very low birefringency, which depends on their orientation, making them difficult to be detected. (*c*) UV-fluorescence image recorded with Korima UV microscope (excitation 280 nm, emission 350 nm). Slight protein precipitation and several protein crystals are clearly seen in this image.

hydrophobic additives may be explored to great effect. These additives can be mixed directly with the host lipid before combining them with the protein solution to form the LCP matrix. We found that cholesterol, an important component of biological membranes in mammalian cells, dramatically improves the size and the quality of β_2AR-T4L and A_{2A}R-T4L crystals grown in LCP (Cherezov *et al.* 2007; Hanson *et al.* 2008; Jaakola *et al.* 2008). To increase the crystal size, it was necessary to concentrate protein between approximately 50 and 70 mg ml^{-1}. At higher protein concentration, the detergent content was too high, causing the LCP to transform into a lamellar phase (Misquitta & Caffrey 2003), which was detrimental to the crystal growth. Another important optimization parameter was the volume of the lipidic mesophase bolus, which reproducibly improved the final crystal size for β_2AR-T4L when decreased from 50 to 20 nl. This phenomenon is likely related to the differences in equilibration times after adding precipitant to the lipidic mesophase, which can range from hours to days depending on the volume of the mesophase bolus and the size of the precipitant molecules. Even after extensive optimization, the *in meso* crystals were still rather small by typical crystallography standards (figure 1*d*), which could be explained by the relatively low stability of GPCRs. Obtaining the most diffraction information from such small crystals required using a high-intensity X-ray beam with a diameter less than 10 μm.

For crystallographic data collection the microcrystals must first be harvested from the LCP. The glass sandwich plates were initially developed for high throughput screening and optimization (Cherezov *et al.* 2004). The wells in these plates were tightly sealed with two glass slides complicating the opening of individual wells for harvesting. Conditions optimized in the glass sandwich plates have been successfully translated into commercial plastic minibatch or vapour diffusion plates to grow harvestable crystals of light harvesting complex II (Cherezov *et al.* 2006*a*), outer membrane vitamin B_{12} transporter BtuB (Cherezov *et al.* 2006*b*) and outer membrane adhesion OpcA (Cherezov *et al.* 2008). However, after performing extensive GPCR crystallization trials in plastic trays, we were not able to obtain similar size and quality crystals as those grown in the glass sandwich plates. The inability to translate the crystal growth conditions into a more traditional plate format triggered the development of a procedure for harvesting crystals directly from the glass sandwich screening plates. Each well containing crystals was accessed by first scoring and removing a small square piece of the cover glass followed by harvesting of the crystals directly from the 20 nl cubic phase bolus. Thus, the utility of the glass sandwich plates was extended and currently all crystals are directly harvested from these plates without the need to translate conditions saving time and protein resources. It has previously been demonstrated that crystals can be released from the LCP gel for harvesting using an enzymatic lipid digestion (Nollert & Landau 1998), detergent solutions (Luecke *et al.* 1999), sponge inducing additives (Cherezov *et al.* 2006*a*) or mineral oils. We observed that in the case of GPCR crystals any of these perturbations decreased the diffraction quality of the harvested crystals. Moreover, it was easier to harvest colourless microcrystals when they were embedded in the LCP gel, rather than free floating in solution. Another benefit of harvesting directly from the LCP was that lipids surrounding the crystal provide additional cryoprotection during the freezing in liquid nitrogen. One major drawback of this approach is that upon freezing, the lipidic mesophase turns opaque rendering the embedded crystals invisible, which complicates data collection (see §3.3). Furthermore, the lipids

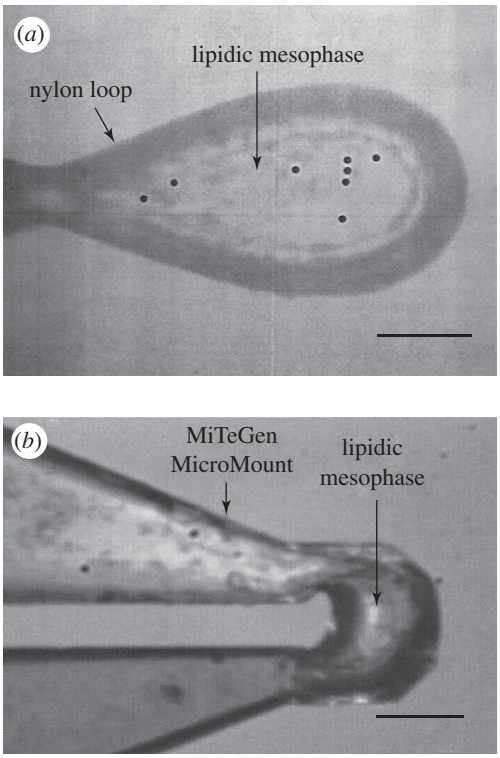

Figure 4. Images of loops with harvested β_2AR-T4L crystals under a cryo-stream recorded through the inline optics at the GM/CA beamline at APS. (*a*) A nylon loop with several optically invisible β_2AR-T4L crystals embedded into a frozen lipidic mesophase. Scanning the loop with the minibeam revealed a distinct protein diffraction at locations marked with the black circles. (*b*) A MiTeGen MicroMount containing a small amount of lipidic mesophase with a single β_2AR-T4L crystal. The crystal is optically invisible but can be easily located using the automated rastering procedure implemented at the GM/CA beamlines. Scale bars, 50 μm.

surrounding the crystal contribute to the background scattering, thus minimizing the amount of mesophase harvested with the crystal is essential for optimal diffraction. We prefer to use MiTeGen MicroMounts (www.mitegen.com) for harvesting as they are thin but sufficiently rigid to easily penetrate the LCP allowing a minimal amount of extraneous lipid when the size of the MicroMount appropriately matches the size of the crystal (figure 4*b*).

3.2. Minibeam development

Approaches to developing microbeams for macromolecular crystallography fall in two major categories. Beamline ID23-2 of the European Synchrotron Source uses short focal length (approx. 1 m) mirrors arranged in Kirkpatrick–Beaz (KB) geometry positioned close to the sample to focus the beam to the desired size (approx. 7 μm). Any movement of the source or mirrors can result in the beam position drifting at the sample position.

The GM/CA CAT beamlines at the APS use long focal length mirrors (approx. 5–8 m) also arranged in a KB geometry to focus the beam to 20–25 × 65–120 μm^2, depending on the particular beamline. A minibeam collimator positions a pin-hole aperture 30 mm upstream of the sample position which defines a 5 or 10 μm beam at the sample position. Experiments prior to February 2008 used single minibeam collimators with either 5 or 10 μm apertures. Some data reported in this paper used a 10 μm pin hole that provided a 7.8 × 6.3 μm^2 (FWHM) beam with an intensity of 1×10^{11} photons s^{-1} $(100\ mA)^{-1}$ (Sanishvili *et al.* 2008). Later experiments used a triple minibeam collimator to position any one of three, user selectable, beam defining, pin-hole apertures (Fischetti *et al.* 2009). The collimator houses 5 and 10 μm beam defining apertures and a 300 μm scatter guard. The 10 μm pin hole provided a $10.6 \times 11.6\ \mu m^2$ beam with an intensity of 2.2×10^{11} photons s^{-1} $(100\ mA)^{-1}$. This later pin hole had a slightly larger diameter than the previous one accounting for the increased beam size and intensity. The minibeams at GM/CA have Gaussian profiles and virtually no tails. The mirrors intercept the full cone of emission from the undulator source on both beamlines providing a high-intensity focused beam at the sample position. A high level of positional and intensity stability of the beam is achieved because of the focused beam being significantly larger than the small pin holes (Fischetti *et al.* 2009). The long focal length mirrors provide a beam with low convergence, which is further reduced by the pin-hole apertures.

Beamline X06SA of the Swiss Light Source combines the two approaches such that the beam is focused to the desired size in the vertical direction and defined in the horizontal direction using the beam shaper of the MD-2 micro-diffractometer (Perrakis *et al.* 1999; Cipriani *et al.* 2007).

3.3. Loop rastering, crystal location and centring

GPCR microcrystals, harvested directly from the LCP and frozen in liquid nitrogen, were invisible through the beamline optics (figure 4). To locate the crystals in the loops and precisely align them with the 10 μm minibeam, we have developed an approach using diffraction from a highly attenuated beam of variable size as a probe (see §2.4). Applying this procedure manually was rather tedious taking 30–60 min to align each crystal. This inconvenience prompted development and implementation of an automatic rastering utility, which was fully integrated in the beamline controlling software (Blu-Ice; figure 5). With this routine, the crystal alignment time decreased to approximately 10 min, significantly increasing the throughput of screening for optimal diffraction.

3.4. Radiation damage

Collecting high-resolution data from small microcrystals requires exposing them to a higher X-ray dose, inevitably leading to increased radiation damage. It was suggested that a twofold decrease in diffraction intensity during data collection owing to the radiation damage is tolerable (Henderson 1990; Owen *et al.* 2006; Holton 2009). Such decay can be partially compensated for computationally (Diederichs 2006) and

typically will not introduce significant errors in the electron density. Henderson estimated the limiting X-ray dose that destroys half of the diffraction intensity in any protein crystal as 20 MGy (Henderson 1990). Recently, more comprehensive studies on seven approximately 200 μm crystals extended this number to 43 MGy and suggested an upper dose limit of 30 MGy for data collection (Owen *et al.* 2006). These estimates should, of course, be followed with caution as different crystals may have different sensitivities to the damage (Holton 2009). In the case of micrometre-size crystals, theoretical calculations predict that the radiation damage could be significantly lower owing to an escape of the secondary electrons from the crystal (Nave & Hill 2005); a systematic experimental study to test these predictions is currently under way (R. F. Fischetti and R. Sanishvili 2009, unpublished data).

We measured the decrease in the diffracted intensity in different resolution shells owing to radiation damage for a small microcrystal of A_{2A}R-T4L ($40 \times 15 \times 3\ \mu m^3$; figure 6). As expected, the higher resolution reflections decay faster, making it increasingly more difficult to collect higher resolution data from microcrystals. Several authors estimated the minimum size of the crystal, from which it is possible to collect a full dataset, as approximately 20–30 μm in all three dimensions (Glaeser *et al.* 2000; Teng & Moffat 2000; Sliz *et al.* 2003). As all our crystals were on average of smaller size, we had to use multiple crystals to collect a complete dataset. While working with the *in meso* grown β_2AR-T4L microcrystals of typical size $25 \times 8 \times 4\ \mu m^3$, we empirically established the following correlations between the beam intensity, the amount of collected data and the achieved maximal resolution: using 1 s exposures with 20-fold attenuated beam and 1° oscillation allowed one to collect approximately 200° of data with resolution of approximately 5–6 Å, corresponding to a total absorbed X-ray dose of approximately 10 MGy (calculated with the RADDOSE program; Murray *et al.* 2004); using 1 s exposures with fivefold attenuation and 1° oscillation allowed one to collect 40° with resolution approximately 3–3.5 Å (total absorbed X-ray dose of approximately 8 MGy); using 1 s exposures without attenuation and 1° oscillation allowed one to collect 7° with resolution approximately 2.5 Å (total absorbed X-ray dose approx. 7 MGy); and, finally, using 5 s exposures without attenuation and 1° oscillation allowed one to collect just one frame with resolution approximately 2.2 Å (total absorbed X-ray dose approx. 5 MGy). The actual resolution would of course vary from crystal to crystal and the final determination for useable resolution and amount of data was ultimately based on scaling statistics after incorporation of each wedge of data into the main dataset.

3.5. Data collection strategies

Because radiation damage limits the collection of full datasets from small crystals, one has to carefully design the data collection strategy. Several strategies have been recently applied to mitigate the effect of radiation damage on data collected from crystals with small volumes (Coulibaly *et al.* 2007; Moukhametzianov *et al.* 2008). The strategy applied here combined a low-resolution (4–5 Å) full dataset recorded from a single crystal with high-resolution (2.2–2.8 Å) wedges collected from multiple crystals. The low-resolution data served as a reference set for scaling the small wedges of high-resolution data. When enough wedges were collected to assemble a complete dataset, the low-resolution set was removed from the final data.

To optimize the collection of high-resolution data, we first estimated the maximum obtainable diffraction limit. Although the best crystals diffracted to about 2.0 Å or better using 5–10 s exposure with unattenuated beam, the majority of them fell in the 2.0–2.5 Å resolution range. Therefore, we took a conservative approach of taking 1 s exposures per frame, which allowed us to collect 10–15 usable frames with 1° oscillation from each crystal. Merging data from multiple crystals relies on the crystal isomorphism. The *in meso* grown GPCR crystals did provide such isomorphism in contrast to often highly non-isomorphic crystals of membrane proteins grown in detergent solutions (Carpenter *et al.* 2008). While it is possible to merge just single frames from hundreds of crystals (Grimes *et al.* 1998), the data quality certainly suffers as the number of frames collected from each crystal decreases. We have found empirically that 10–15 frames per crystal provided the best compromise between data quality and resolution for the type and size of crystals we were using. Initially, the high-resolution data wedges were collected starting from the same loop orientation assuming random orientation of crystals in the loop. This approach worked well with β_2AR-T4L crystals. However, in the case of A_{2A}R-T4L this resulted in systematic omission of reflections at certain orientations. Using the strategy to select the starting angles for the high-resolution wedges as implemented in XDS (Kabsch 1993) helped to collect a complete dataset. In order to minimize the radiation damage from the X-ray exposure during this procedure, we attenuated the beam 10-fold and based our prediction on diffraction data at a maximal resolution of 4–5 Å. We found that collecting an initial wedge of 5–10 frames resulted in a more reliable indexing of the low-resolution diffraction images allowing an assignment of the orientation matrix and prediction of the best rotation angle to add completeness to the high-resolution dataset.

The data collected from multiple crystals were processed and scaled with XDS (Kabsch 1993). XDS can account for the radiation damage (Diederichs 2006) and compensate for the movement of the crystal out of the beam due to small deviations of the rotation axis from the crystal centre. The final data collection and scaling statistics are shown in table 1. Data from 27 crystals were merged together to obtain the final dataset for β_2AR-T4L/carazolol structure. For β_2AR(E122W)-T4L/timolol and A_{2A}R-T4L/ZM241385, 11 and 13 crystals were used, respectively. Fewer crystals were required in the last two cases because of the higher symmetry space group and lower resolution. In practice, at least two times more data were collected in each case. The high-resolution data wedges that did not scale well with the low-resolution set, representing less than 20 per cent of all crystals, were discarded. The best

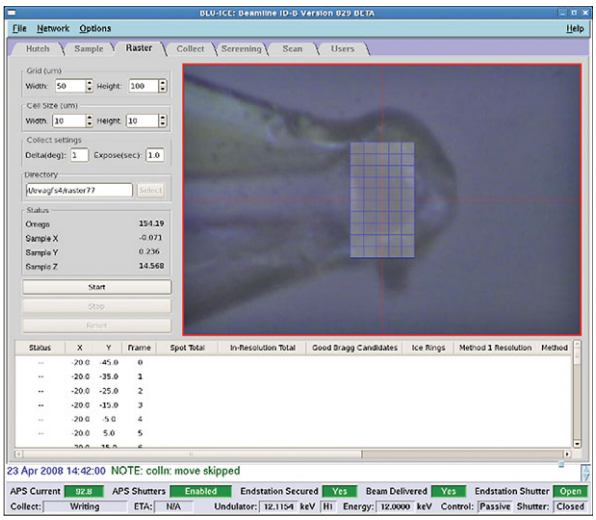

Figure 5. A screenshot of the automated rastering interface window in Blu-Ice. After centring the loop at the crosshair, the user defines a grid for rastering, selects exposure parameters at each cell of the grid and starts the scan. Collected diffraction frames are processed in real time using the program DISTL (Zhang *et al.* 2006) and the results are displayed in the window at the lower part of the screen.

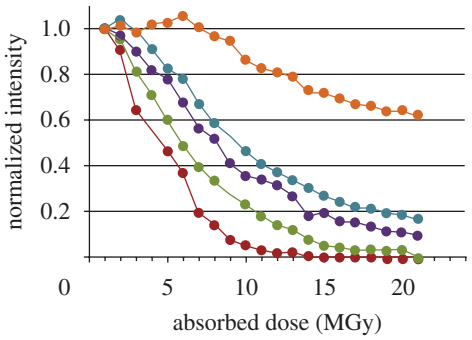

Figure 6. Effect of radiation damage on the intensity of diffraction spots collected in different resolution shells (identified as different colours) from a crystal of A_{2A}R-T4L. The crystal was exposed multiple times at the same orientation with the unattenuated minibeam using the 1° oscillation and 1 s exposure per frame. Each frame corresponds to an estimated radiation dose of 1 MGy absorbed by the crystal (the dose was calculated using the program RADDOSE; Murray *et al.* 2004). The crystal lost half of its diffraction intensity at 3 Å resolution after absorbing approximately 5 MGy. Red line, 3–3.1 Å; green line, 4–4.2 Å; violet line, 6–6.5 Å; blue line, 7.5–8 Å; orange line, 9–12 Å.

Table 1. Data collection statistics (data for the highest resolution shell are shown in parentheses).

protein	β_2AR-T4L	β_2AR(E122W)-T4L	A_{2A}R-T4L
ligand	carazolol	timolol	ZM241385
PDB ID	2RH1	3D4S	3EML
space group	C2	$P2_12_12_1$	$P2_1$
number of crystals	27	11	13
cell dimensions			
a, *b*, *c* (Å)	106.3, 169.2, 40.2	40.0, 75.7, 172.7	47.7, 76.9, 86.6
α, β, γ (°)	90, 105.6, 90	90, 90, 90	90, 101.3, 90
total reflections	245 571	54 405	64 526
unique reflections	26 574	12 782	18 465
resolution (Å)	50−2.4 (2.5−2.4)	50−2.8 (3.0−2.8)	20−2.6 (2.8−2.6)
R_{merge}	12.7 (67.8)	14.3 (56.9)	9.8 (38.9)
I/σ	9.6 (2.2)	6.9 (1.9)	7.0 (2.3)
redundancy	9.4 (4.8)	4.2 (2.9)	3.5 (2.3)
completeness (%)	99.5 (99.1)	94.0 (91.0)	96.8 (93.9)

combinations of the high-resolution data providing the lowest R_{merge} and the highest completeness were selected to represent the final merged data. The quality of the final data was very good with the total R_{merge} ranging between 10 and 15 per cent.

3.6. Summary of G protein-coupled receptor structure results

Structure of β_2AR-T4L bound to diffusible ligand carazolol was solved by molecular replacement (Cherezov *et al.* 2007). Initial solution was found by Phaser (McCoy 2007) using a polyalanine model of seven TM helices of rhodopsin (PDB ID 1U19) together with a model of T4 lysozyme. Subsequent structures of β_2AR(E122W)-T4L/timolol (Hanson *et al.* 2008) and A_{2A}R-T4L/ZM241385 (Jaakola *et al.* 2008) were also solved by molecular replacement using separated structures of β_2AR and T4L from the first β_2AR-T4L/carazolol structure (PDB ID 2RH1) as the search models.

All three structures are composed of a seven TM bundle and a short helix 8 running along the membrane at the cytoplasmic side (figure 7). Structural alignments of the rhodopsin, β_2AR and A_{2A}R backbones reveal slight shifts, rotations and twists between the corresponding helices, resulting in mutual displacements ranging between 1 and 7 Å depending on the helix and on the position of the residue in the helix. Rotations and twists occur mostly around conserved proline residues. The most divergent part of the seven TM bundle is at the extracellular side, around the ligand binding site. In contrast to rhodopsin, in which the N-terminus together with the second extracellular loop (ECL2) form a four-stranded beta-sheet, closing access to the ligand from the extracellular side, in both β_2AR-T4L and A_{2A}R-T4L the N-terminus is disordered and the ECL2 is shaped with disulphide bonds (two disulphides in β_2AR-T4L and four disulphides in A_{2A}R-T4L) so that the passage to the

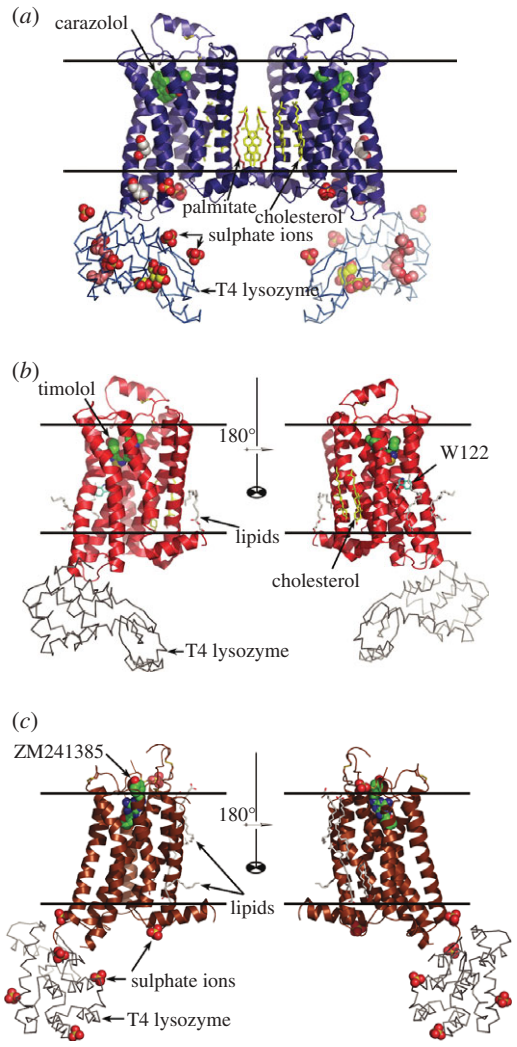

Figure 7. Crystal structures of (*a*) β_2AR-T4L bound to carazolol (PDB ID 2RH1; Cherezov *et al.* 2007), (*b*) β_2AR(E122W)-T4L bound to timolol (PDB ID 3D4S; Hanson *et al.* 2008) and (*c*) A_{2A}R-T4L bound to ZM241385 (PDB ID 3EML; Jaakola *et al.* 2008). β_2AR-T4L/carazolol crystallized as a parallel crystallographic dimer as shown in (*a*). Both β_2AR(E122W)-T4L/timolol and A_{2A}R-T4L/ZM241385 crystallized as monomers, and, therefore, two monomers rotated 180° around the vertical axis are shown in (*b*) and (*c*). Approximate locations of the lipid membrane boundaries are shown with two parallel black lines. Receptors are oriented with their extracellular side facing the top of the figure.

ligand binding site is open for diffusible ligand. The ligand binding sites and interactions of ligands with receptors' residues are well defined in all solved structures. Binding modes of β_2AR antagonists carazolol and timolol are similar to each other, and their orientations and locations with respect to the receptors resemble those of retinal in rhodopsin. The A_{2A}R antagonist ZM241385, however, binds in an unexpected, orthogonal to the membrane plane orientation. In both β_2AR and A_{2A}R, the ligands substantially interact with residues on ECL2. Loop conformations and thus these interactions are difficult to predict.

In addition to establishing high-resolution snapshots of two GPCRs bound to diffusible antagonists, the new structures are invaluable in providing high-quality templates for generating models of closely related receptors suitable for virtual ligand screening (Katritch *et al.* 2009; Reynolds *et al.* 2009). The work on expanding the coverage of the diverse GPCR structural space, as well as pursuit towards the activated receptor state, is in progress.

4. CONCLUSIONS

Technology developments in membrane protein crystallization and synchrotron microcrystallography combined with advancements in protein stabilization and purification have enabled structural determination of two members of the pharmaceutically important and highly challenging family of GPCRs. Highly ordered, yet small ($<1000\ \mu m^3$), microcrystals of engineered human $\beta 2$ adrenergic and adenosine A_{2A} receptors bound to diffusible ligands were obtained through utilization of high-throughput robotic crystallization techniques in lipidic mesophases. Development of the minibeam instrumentation and rastering software by the GM/CA CAT at the Advance Photon Source allowed for high-quality crystallographic data collection from multiple GPCR microcrystals. Using the 10 μm minibeam substantially improved the signal-to-noise ratio of collected reflections and extended the resolution, when compared with conventional beams defined by slits. Data collection from microcrystals with the minibeam was limited by the radiation damage. Obtaining maximum structural information from available microcrystals at a minimal damage level required careful planning and optimization of data collection strategies. Further decrease in the synchrotron beam size may provide intriguing opportunities for improving data quality and mitigating radiation damage.

This work was supported in part by the NIH Roadmap Initiative grant P50 GM073197 and Protein Structure Initiative grant U54 GM074961. The authors acknowledge D. Rosenbaum and B. Kobilka from Stanford University for providing initial β_2AR-T4L samples, crystals of which were used to develop some of the approaches described in this paper, as well as Y. Zheng, Ohio State University, and M. Caffrey, University of Limerick, for the generous loan of the *in meso* robot (built with support from the NIH (GM075915), the NSF (IIS0308078) and Science Foundation Ireland (02-IN1-B266)). The GM/CA CAT beamline (23-ID) is supported by the National Cancer Institute (Y1-CO-1020) and the National Institute of General Medical Sciences (Y1-GM-1104).

REFERENCES

Adams, P. D. *et al.* 2002 PHENIX: building new software for automated crystallographic structure determination. *Acta Crystallogr. D Biol. Crystallogr.* **58**, 1948–1954. (doi:10.1107/S0907444902016657)

Benvenuti, M. & Mangani, S. 2007 Crystallization of soluble proteins in vapor diffusion for x-ray crystallography. *Nat. Protoc.* **2**, 1633–1651. (doi:10.1038/nprot.2007.198)

Caffrey, M. 2003 Membrane protein crystallization. *J. Struct. Biol.* **142**, 108–132. (doi:10.1016/S1047-8477(03)00043-1)

Caffrey, M. 2009 Crystallizing membrane proteins for structure determination: use of lipidic mesophases. *Annu. Rev.*

Biophys. **38**, 29–51. (doi:10.1146/annurev.biophys.050708.133655)

Carpenter, E. P., Beis, K., Cameron, A. D. & Iwata, S. 2008 Overcoming the challenges of membrane protein crystallography. *Curr. Opin. Struct. Biol.* **18**, 581–586. (doi:10.1016/j.sbi.2008.07.001)

Cheng, A., Hummel, B., Qiu, H. & Caffrey, M. 1998 A simple mechanical mixer for small viscous lipid-containing samples. *Chem. Phys. Lipids* **95**, 11–21. (doi:10.1016/S0009-3084(98)00060-7)

Cherezov, V., Peddi, A., Muthusubramaniam, L., Zheng, Y. F. & Caffrey, M. 2004 A robotic system for crystallizing membrane and soluble proteins in lipidic mesophases. *Acta Crystallogr. D Biol. Crystallogr.* **60**, 1795–1807. (doi:10.1107/S0907444904019109)

Cherezov, V., Clogston, J., Papiz, M. Z. & Caffrey, M. 2006*a* Room to move: crystallizing membrane proteins in swollen lipidic mesophases. *J. Mol. Biol.* **357**, 1605–1618. (doi:10.1016/j.jmb.2006.01.049)

Cherezov, V., Yamashita, E., Liu, W., Zhalnina, M., Cramer, W. A. & Caffrey, M. 2006*b* *In meso* structure of the cobalamin transporter, BtuB, at 1.95 Å resolution. *J. Mol. Biol.* **364**, 716–734. (doi:10.1016/j.jmb.2006.09.022)

Cherezov, V. *et al.* 2007 High-resolution crystal structure of an engineered human beta2-adrenergic G protein-coupled receptor. *Science* **318**, 1258–1265. (doi:10.1126/science.1150577)

Cherezov, V., Liu, W., Derrick, J. P., Luan, B., Aksimentiev, A., Katritch, V. & Caffrey, M. 2008 *In meso* crystal structure and docking simulations suggest an alternative proteoglycan binding site in the OpcA outer membrane adhesion. *Proteins* **71**, 24–34. (doi:10.1002/prot.21841)

Cipriani, F., Felisaz, F., Lavault, B., Brockhauser, S., Ravelli, R., Launer, L., Leonard, G. & Renier, M. 2007 *9th Int. Conf. Synchrotron Radiation Instrumentation* (eds J.-Y. Choi & S. Rah), pp. 1928–1931. New York, NY: American Institute of Physics.

Coulibaly, F., Chiu, E., Ikeda, K., Gutmann, S., Haebel, P. W., Schulze-Briese, C., Mori, H. & Metcalf, P. 2007 The molecular organization of cypovirus polyhedral. *Nature* **446**, 97–101. (doi:10.1038/nature05628)

Diederichs, K. 2006 Some aspects of quantitative analysis and correction of radiation damage. *Acta Crystallogr. D Biol. Crystallogr.* **62**, 96–101. (doi:10.1107/S0907444905031537)

Emsley, P. & Cowtan, K. 2004 Coot: model-building tools for molecular graphics. *Acta Crystallogr. D Biol. Crystallogr.* **60**, 2126–2132. (doi:10.1107/S0907444904019158)

Fischetti, R. F. *et al.* 2009 Mini-beam collimator enables microcrystallography experiments on standard beamlines. *J. Synchrotron Radiat.* **16**, 217–225. (doi:10.1107/S0909049508040612)

Glaeser, R., Facciotti, M., Walian, P., Rouhani, S., Holton, J., MacDowell, A., Celestre, R., Cambie, D. & Padmore, H. 2000 Characterization of conditions required for X-ray diffraction experiments with protein microcrystals. *Biophys. J.* **78**, 3178–3185. (doi:10.1016/S0006-3495(00)76854-8)

Grimes, J. M., Burroughs, J. N., Gouet, P., Diprose, J. M., Malby, R., Zientara, S., Mertens, P. P. & Stuart, D. I. 1998 The atomic structure of the bluetongue virus core. *Nature* **395**, 470–478. (doi:10.1038/26694)

Hanson, M. A., Cherezov, V., Griffith, M. T., Roth, C. B., Jaakola, V. P., Chien, E. Y., Velasquez, J., Kuhn, P. & Stevens, R. C. 2008 A specific cholesterol binding site is established by the 2.8 Å structure of the human beta(2)-adrenergic receptor. *Structure* **16**, 897–905. (doi:10.1016/j.str.2008.05.001)

Henderson, R. 1990 Cryo-protection of protein crystals against radiation damage in electron and X-ray diffraction. *Proc. R. Soc. Lond. B* **241**, 6–8. (doi:10.1098/rspb.1990.0057)

Holton, J. M. 2009 A beginner's guide to radiation damage. *J. Synchrotron Radiat.* **16**, 133–142. (doi:10.1107/S0909049509004361)

Jaakola, V. P., Griffith, M. T., Hanson, M. A., Cherezov, V., Chien, E. Y., Lane, J. R., Ijzerman, A. P. & Stevens, R. C. 2008 The 2.6 angstrom crystal structure of a human A2A adenosine receptor bound to an antagonist. *Science* **322**, 1211–1217. (doi:10.1126/science.1164772)

Kabsch, W. 1993 Automatic processing of rotation diffraction data from crystals of initially unknown symmetry and cell constants. *J. Appl. Cryst.* **26**, 795–800. (doi:10.1107/S0021889893005588)

Katritch, V., Cherezov, V., Hanson, M. A., Roth, R. B., Yeager, M. & Abagyan, R. 2009 Analysis of full and partial agonists binding to beta(2)-adrenergic receptor suggests a role of transmembrane helix V in agonist-specific conformational changes. *J. Mol. Recognit.* **22**, 307–318. (doi:10.1002/jmr.949)

Landau, E. M. & Rosenbusch, J. P. 1996 Lipidic cubic phases: a novel concept for the crystallization of membrane proteins. *Proc. Natl Acad. Sci. USA* **93**, 14 532–14 535. (doi:10.1073/pnas.93.25.14532)

Luecke, H., Schobert, B., Richter, H. T., Cartailler, J. P. & Lanyi, J. K. 1999 Structure of bacteriorhodopsin at 1.55 Å resolution. *J. Mol. Biol.* **291**, 899–911. (doi:10.1006/jmbi.1999.3027)

McCoy, A. J. 2007 Solving structures of protein complexes by molecular replacement with Phaser. *Acta Crystallogr. D Biol. Crystallogr.* **63**, 32–41. (doi:10.1107/S0907444906045975)

McPhillips, T. M. *et al.* 2002 Blu-Ice and the Distributed Control System: software for data acquisition and instrument control at macromolecular crystallography beamlines. *J. Synchrotron Radiat.* **9**, 401–406. (doi:10.1107/S0909049502015170)

Misquitta, Y. & Caffrey, M. 2003 Detergents destabilize the cubic phase of monoolein: implications for membrane protein crystallization. *Biophys. J.* **85**, 3084–3096. (doi:10.1016/S0006-3495(03)74727-4)

Moukhametzianov, R., Burghammer, M., Edwards, P. C., Petitdemange, S., Popov, D., Fransen, M., McMullan, G., Schertler, G. F. & Riekel, C. 2008 Protein crystallography with a micrometre-sized synchrotron-radiation beam. *Acta Crystallogr. D Biol. Crystallogr.* **64**, 158–166. (doi:10.1107/S090744490705812X)

Murray, J. W., Garman, E. F. & Ravelli, R. B. G. 2004 X-ray absorption by macromolecular crystals: the effects of wavelength and crystal composition on absorbed dose. *J. Appl. Cryst.* **37**, 513–522. (doi:10.1107/S0021889804010660)

Murshudov, G. N., Vagin, A. A. & Dodson, E. J. 1997 Refinement of macromolecular structures by the maximum-likelihood method. *Acta Crystallogr. D Biol. Crystallogr.* **53**, 240–255. (doi:10.1107/S0907444996012255)

Nave, C. & Hill, M. A. 2005 Will reduced radiation damage occur with very small crystals? *J. Synchrotron Radiat.* **12**, 299–303. (doi:10.1107/S0909049505003274)

Nollert, P. & Landau, E. M. 1998 Enzymic release of crystals from lipidic cubic phases. *Biochem. Soc. Trans.* **26**, 709–713.

Owen, R. L., Rudino-Pinera, E. & Garman, E. F. 2006 Experimental determination of the radiation dose limit for cryocooled protein crystals. *Proc. Natl Acad. Sci. USA* **103**, 4912–4917. (doi:10.1073/pnas.0600973103)

Pebay-Peyroula, E., Rummel, G., Rosenbusch, J. P. & Landau, E. M. 1997 X-ray structure of bacteriorhodopsin at 2.5 angstroms from microcrystals grown in lipidic

cubic phases. *Science* **277**, 1676–1681. (doi:10.1126/science.277.5332.1676)

Perrakis, A., Cipriani, F., Castagna, J.-C., Claustre, L., Burghammer, M., Riekel, C. & Cusack, S. 1999 Protein microcrystals and the design of a microdiffractometer: current experience and plans at EMBL and ESRF/ID13. *Acta Crystallogr. D Biol. Crystallogr.* **55**, 1765–1770. (doi:10.1107/S0907444999009348)

Rasmussen, S. G. *et al.* 2007 Crystal structure of the human beta2 adrenergic G-protein-coupled receptor. *Nature* **450**, 383–387. (doi:10.1038/nature06325)

Reynolds, K. A., Katritch, V. & Abagyan, R. 2009 Identifying conformational changes of the beta(2) adrenoceptor that enable accurate prediction of ligand/receptor interactions and screening for GPCR modulators. *J. Comput. Aided Mol. Des.* **23**, 273–288. (doi:10.1007/s10822-008-9257-9)

Rosenbaum, D. M. *et al.* 2007 GPCR engineering yields high-resolution structural insights into beta2-adrenergic receptor function. *Science* **318**, 1266–1273. (doi:10.1126/science.1150609)

Roth, C. B., Hanson, M. A. & Stevens, R. C. 2008 Stabilization of the human beta2-adrenergic receptor TM4–TM3–TM5 helix interface by mutagenesis of Glu122(3.41), a critical residue in GPCR structure. *J. Mol. Biol.* **376**, 1305–1319. (doi:10.1016/j.jmb.2007.12.028)

Sanishvili, R., Nagarajan, V., Yoder, D., Becker, M., Xu, S., Corcoran, S., Akey, D. L., Smith, J. L. & Fischetti, R. F. 2008 A 7 microm mini-beam improves diffraction data from small or imperfect crystals of macromolecules. *Acta Crystallogr. D Biol. Crystallogr.* **64**, 425–435. (doi:10.1107/S0907444908001741)

Sliz, P., Harrison, S. C. & Rosenbaum, G. 2003 How does radiation damage in protein crystals depend on X-ray dose? *Structure* **11**, 13–19. (doi:10.1016/S0969-2126(02)00910-3)

Song, J., Mathew, D., Jacob, S. A., Corbett, L., Moorhead, P. & Soltis, S. M. 2007 Diffraction-based automated crystal centering. *J. Synchrotron Radiat.* **14**, 191–195. (doi:10.1107/S0909049507004803)

Stepanov, S., Makarov, O., Urakhchin, A., Devarapalli, S., Yoder, D. & Fischetti, R. 2006 GM/CA CAT beamline control system for protein crystallography at the APS. In *NOBUGS-2006 Conf. Program & Abstracts*, *LBL, Berkeley, CA*, *2–4 October 2006*, pp. 31–32.

Teng, T. Y. & Moffat, K. 2000 Primary radiation damage of protein crystals by an intense synchrotron X-ray beam. *J. Synchrotron Radiat.* **7**, 313–317. (doi:10.1107/S0909049500008694)

Xiao, B. *et al.* 2003 Crystal structure of the retinoblastoma tumor suppressor protein bound to E2F and the molecular basis of its regulation. *Proc. Natl Acad. Sci. USA* **100**, 2363–2368. (doi:10.1073/pnas.0436813100)

Zhang, Z., Sauter, N. K., van den Bedem, H., Snell, G. & Deacon, A. M. 2006 Automated diffraction image analysis and spot searching for high-throughput crystal screening. *J. Appl. Cryst.* **39**, 112–119. (doi:10.1107/S0021889805040677)